Journal of Materials Chemistry A

ROYAL SOCIETY OF CHEMISTRY

PAPER

View Article Online
View Journal | View Issue

Cite this: J. Mater. Chem. A, 2022, 10, 10692

Na-β-Al_2O_3 stabilized Fe_2O_3 oxygen carriers for chemical looping water splitting: correlating structure with redox stability†

Nur Sena Yüzbasi, [a] Andac Armutlulu, [a] Thomas Huthwelker,[b] Paula M. Abdala *[a] and Christoph R. Müller *[a]

Received 8th December 2021
Accepted 11th April 2022

DOI: 10.1039/d1ta10507h

rsc.li/materials-a

Chemical looping is an emerging technology to produce high purity hydrogen from fossil fuels or biomass with the simultaneous capture of the CO_2 produced at the distributed scale. This process requires the availability of stable Fe_2O_3-based oxygen carriers. Fe_2O_3–Al_2O_3 based oxygen carriers exhibit a decay in the H_2 yield with cycle number, due to the formation of $FeAl_2O_4$ that possesses a very low capacity for water splitting at typical operating conditions of conventional chemical looping schemes (700–1000 °C). In this study, the addition of sodium (*via* a sodium salt) in the synthesis of Fe_2O_3–Al_2O_3 oxygen carriers was assessed as a means to counteract the cyclic deactivation of the oxygen carrier. Detailed insight into the oxygen carrier's structure was gained by combined X-ray powder diffraction (XRD), X-ray absorption spectroscopy (XAS) at the Al, Na and Fe K-edges and scanning transmission electron microscopy/energy-dispersive X-ray spectroscopy (STEM/EDX) analyses. The addition of sodium prevented the formation of $FeAl_2O_4$ and stabilized the oxygen carrier *via* the formation of a layered structure, Na-β-Al_2O_3 phase. The material, *i.e.* Na-β-Al_2O_3 stabilized Fe_2O_3, showed a stable H_2 yield of *ca.* 13.3 mmol g^{-1} over 15 cycles.

Introduction

Hydrogen is an emerging energy carrier with potential applications in the transport, industry and power sectors as a fuel that yields water vapour as the only combustion product. If produced sustainably, H_2 has the potential to become a near-zero emissions energy carrier, hence reducing energy-related CO_2 emissions.[1–3] Currently, the majority of H_2 is produced from natural gas *via* steam methane reforming (SMR) without carbon dioxide capture, which is an energy intensive process and emits a significant amount of CO_2.[3,4] In addition, further energy-intensive purification steps are required to obtain H_2 of sufficiently high purity allowing its use in polymer electrolyte membrane fuel cells (PEMFC).[5,6] Hence, for H_2 to become an energy carrier in a sustainable framework, it must be produced in an efficient and sustainable manner, *i.e.* from renewable sources or with CO_2 capture.[7,8]

A chemical looping (CL) scheme based on the cyclic redox reactions of iron oxide/iron offers the possibility to produce high purity H_2 with inherent CO_2 capture (Fig. 1a).[7–14] This process could be operated using different reducing gases such as CO, synthesis gas (produced by biomass gasification) or natural gas.[15,16] For instance, CO is used to reduce Fe_2O_3 to lower oxidation states (ideally to metallic Fe which gives the highest H_2 yield), following reactions (1)–(3). During Fe_2O_3 reduction, a pure stream of CO_2 is obtained readily through the condensation of water vapour. The oxidation of metallic Fe with steam produces H_2 (water splitting reactions (4) and (5)) of high purity.[17] To close the cycle, Fe_3O_4 is oxidized to Fe_2O_3 in air (reaction (6)).

Reduction of iron oxide in CO

$$3Fe_2O_3 + CO \leftrightarrow 2Fe_3O_4 + CO_2 \quad (1)$$

$$Fe_3O_4 + CO \leftrightarrow 3FeO + CO_2 \quad (2)$$

$$FeO + CO \leftrightarrow Fe + CO_2 \quad (3)$$

Oxidation in steam

$$Fe + H_2O \leftrightarrow FeO + H_2 \quad (4)$$

$$3FeO + 4H_2O \leftrightarrow Fe_3O_4 + 4H_2 \quad (5)$$

Oxidation in air

$$2Fe_3O_4 + \tfrac{1}{2}O_2 \rightarrow 3Fe_2O_3 \quad (6)$$

[a]Laboratory of Energy Science and Engineering, ETH Zurich, Leonhardstrasse 27, 8092, Zurich, Switzerland. E-mail: abdalap@ethz.ch; muelchri@ethz.ch

[b]Swiss Light Source, Paul Scherrer Institut, 5232, Villigen PSI, Switzerland

† Electronic supplementary information (ESI) available. See https://doi.org/10.1039/d1ta10507h

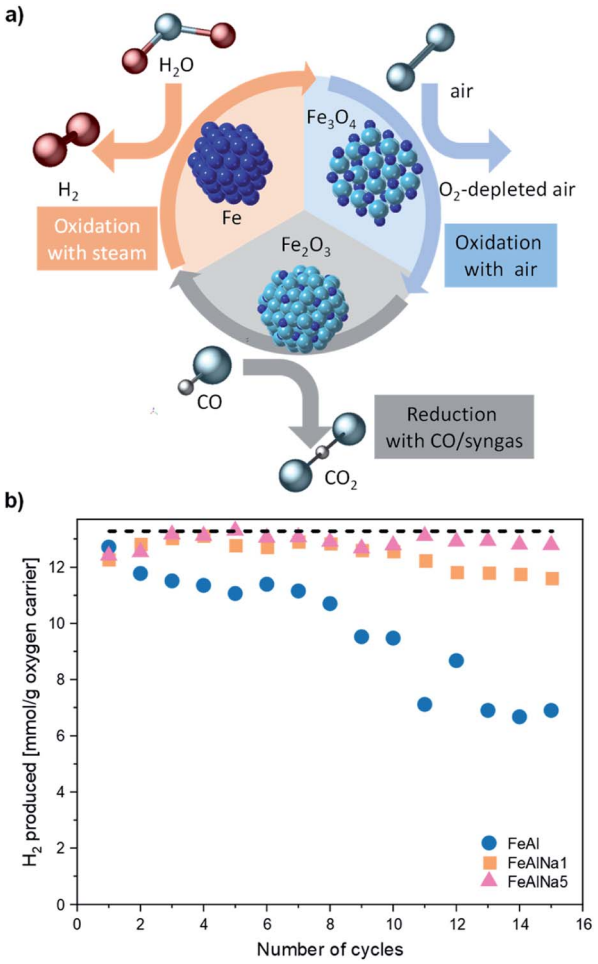

Fig. 1 (a) Schematic of the Fe_2O_3–Fe based chemical looping process for the production of H_2 using a synthesis gas (H_2 and CO) as the fuel. (b) H_2 yield as a function of cycle number for FeAl, FeAlNa1 and FeAlNa5. The redox experiments were performed at 800 °C in a packed-bed reactor using 10 vol% CO in N_2 for reduction and 23 vol% H_2O in N_2 followed by 5 vol% O_2 in N_2 for re-oxidation. The dashed horizontal line represents the theoretically expected H_2 yield (13.3 mmol g^{-1}) for an oxygen carrier that contains 80 wt% Fe_2O_3.

Owing to its favourable thermodynamics iron oxide is one of the most attractive oxygen carriers for the chemical-looping based production of hydrogen.[7–11,13,17–27] However, pure Fe_2O_3 shows a rapid decay in its H_2 yield with number of redox cycles owing to sintering.[17] Sintering leads to an appreciable decrease in the reduction rate of iron oxide, which results in an incomplete reduction and in turn a low H_2 yield in the subsequent re-oxidation step.[7,27,28] To mitigate deactivation by sintering, strategies based on the addition of a high Tammann temperature stabilizing oxide, *e.g.* Al_2O_3,[7,10,22,26,29] SiO_2,[7,9] TiO_2,[30] CeO_2,[14] $MgAl_2O_4$ [21,31] and ZrO_2.[13,23,27] have been proposed. Indeed, these oxides have shown to increase the stability of iron based oxygen carriers over multiple cycles by reducing FeO_x/Fe particle sintering.[23] Among the investigated oxides, Al_2O_3 is particularly interesting owing to its relatively low cost, high Tammann temperature of ~885 °C and high mechanical resistance.[32–34] However, Al_2O_3 can react with iron oxide forming the spinel phase $FeAl_2O_4$ (hercynite) which leads to a decay in the H_2 yield due to the limited capacity of $FeAl_2O_4$ to split water at the typical operating conditions of conventional CL (700–1000 °C).[10,22,26,35] Hydrogen production using iron aluminate-based materials has been proposed for solar driven thermochemical cycles that cycles between spinel iron based solid solutions through an oxygen vacancy mediated mechanism; however, this is limited to high steam-to-hydrogen ratios and the H_2 capacity does not exceed 0.5 mmol H_2 per g $FeAl_2O_4$.[36–38]

Approaches to prevent the formation of $FeAl_2O_4$ during redox operation have included the addition of alkali or alkali earth metal oxides to the oxygen carrier, yet the mechanisms behind the mitigation of $FeAl_2O_4$ formation remains elusive.[23,34,39] In particular, the effect of the addition of sodium on the redox performance of Fe_2O_3–Al_2O_3 based oxygen carriers is controversially discussed and the underlying mechanisms at the atomic scale that would explain the improved macroscopic redox performance of such oxygen carriers are currently not well understood. For instance, a previous study proposed that formulations based on Fe_2O_3, Al_2O_3, Na_2O and/or MgO could potentially hinder the formation of $FeAl_2O_4$ by forming $NaAlO_2$ or $MgAl_2O_4$ phases that are thermodynamically more stable.[31] Indeed, X-ray powder diffraction (XRD) analysis confirmed the presence of $NaAlO_2$ and $MgAl_2O_4$ phases in the two studied oxygen carriers with compositions Na : Al : Fe = 0.25 : 0.25 : 0.50 and Na : Mg : Fe : Al = 0.20 : 0.15 : 0.28 : 0.37 (molar ratios). However, it was found that only $MgAl_2O_4$ effectively hindered the formation of inactive $FeAl_2O_4$ while $NaAlO_2$ only partially prevented its formation. This was explained by the gradual replacement of Al^{3+} by Fe^{3+} in $NaAlO_2$ ($NaAl_{1-y}Fe_yO_2$) during redox cycling leading to the formation of free Al_2O_3 that subsequently reacts with FeO_x to form $FeAl_2O_4$. A further study found that the addition of sodium in concentrations below 5 wt% stabilizes the reactivity of Fe_2O_3, yet the structure of the oxygen carriers was not studied in detail.[20,40] Typically, X-ray powder diffraction (XRD) has been applied to identify the phases present in the oxygen carrier, however, this analysis fails at describing the local structure of the materials and it is insensitive to amorphous phases and phases in low concertation. Thus, the fine structural features of Na-modified Fe_2O_3–Al_2O_3 oxygen carriers remain elusive.

As discussed above, a difficulty in improving our understanding of the effect of the addition of sodium to Fe_2O_3–Al_2O_3 on its redox behaviour is the lack of knowledge of the atomic-scale structure of these materials. Thus, this work aims at shedding light on the structure–performance relationships of sodium modified Fe_2O_3–Al_2O_3 oxygen carriers for H_2-production by addressing the following questions: (i) how is the atomic scale structure of Fe_2O_3–Al_2O_3 based oxygen carriers modified by the addition of Na? (ii) what is the Na, Al and Fe environment in the oxygen carrier? and (iii) how does the redox performance relate to the oxygen carriers' structure? To address these questions we performed a detailed structural and redox analysis of sodium modified Fe_2O_3–Al_2O_3 and a sodium free benchmark utilizing XRD and X-ray absorption spectroscopy (XAS) data at the Fe, Al and Na K-edges.

Experimental

Synthesis of the oxygen carriers

Fe_2O_3:Al_2O_3 and Na-modified Fe_2O_3:Al_2O_3 oxygen carriers were synthesized using a sol–gel method[22] with the following compositions: (i) Fe : Al molar ratio: 0.66 : 0.34 (75 wt% Fe_2O_3, 25 wt% Al_2O_3), referred to as FeAl; (ii) Na : Fe : Al = 0.02 : 0.66 : 0.32 (76 wt% Fe_2O_3, 23 wt% Al_2O_3, 1 wt% Na_2O), referred to as FeAlNa1; and (iii) Na : Fe : Al 0.11 : 0.64 : 0.25 (76 wt% Fe_2O_3, 19% wt% Al_2O_3 and 5 wt% Na_2O), referred to as FeAlNa5, (Table S1†). In a typical synthesis, aluminum isopropoxide ($Al(OCH(CH_3)_2)_3$, purity ≥ 98 wt%) was mixed with water and the mixture was hydrolysed for two hours at 75 °C under constant stirring. Nitric acid was used to peptize the slurry. The required amount of the iron and sodium precursors, iron nitrate ($Fe(NO_3)_3 \cdot 9H_2O$, purity ≥ 98 wt%) and sodium nitrate ($NaNO_3$, purity ≥ 99 wt%) respectively, were mixed with water to obtain a 1 M solution that was added subsequently to the slurry and refluxed for 12 h at 90 °C. The molar ratio of Al^{3+} : H_2O : H^+ was fixed to 0.5 : 50 : 0.07. The resulting gel was dried at 100 °C overnight to remove the solvents. A xerogel was obtained after calcination at 900 °C for 2 hours. The calcined materials were crushed and sieved to a particle size range of 300–425 μm for further characterization.

Reference materials for structural characterization

The following reference materials for XAS analysis were synthesized. Na-β-Al_2O_3, with a molar ratio of Na : Al = 1 : 11 ($NaAl_{11}O_{17}$, $P6_3/mmc$ space group[39]) was synthesized by mixing stoichiometric amounts of γ-Al_2O_3 and Na_2CO_3 followed by calcination at 1350 °C for 6 hours. Na-γ-Al_2O_3 (sodium dispersed at the surface of γ-Al_2O_3) with a molar ratio of Na : Al = 1 : 15 was synthesized by wet impregnation of a solution of $NaNO_3$ (purity > 99 wt%) onto γ-Al_2O_3. The material was dried at 100 °C in an oven overnight, followed by calcination at 900 °C for 2 h. In addition, commercially available α-Al_2O_3 (Alfa Aesar, aluminum oxide, α-phase, 99.9% metal basis) and γ-Al_2O_3 (Alfa Aesar, aluminum oxide, γ-phase, 99.98% metal basis) were utilized as reference materials. The XRD pattern of the references Na-β-Al_2O_3, Na-γ-Al_2O_3, α-Al_2O_3 and γ-Al_2O_3 are provided in Fig. S1.† All of the materials were exposed to ambient conditions before characterization. Thus, ambient humidity likely hydrated the surface of all studied oxygen carriers and references, and possibly also the interlayers in the case of Na-β-Al_2O_3.

Characterization of the oxygen carriers

The crystalline phases of the calcined and cycled oxygen carriers were studied by XRD, using a PANalytical Empyrean X-ray powder diffractometer, equipped with a X'Celerator Scientific ultra-fast line detector and Bragg–Brentano HD incident beam optics using Cu K_α radiation (45 kV and 40 mA). A secondary monochromator was employed to suppress unwanted fluorescence originating from iron. Patterns were collected in the range of 2θ = 5–90°, with a step size of 0.016° s^{-1} and a total acquisition time of 4 h. Rietveld refinements were performed using FullProf software.[41]

The local structure of the materials was characterized by XAS at the Fe, Na and Al K-edges. The Na K-edge and Al K-edge XAS measurements were carried out at the Phoenix II, elliptical undulator beamline at the Swiss Light Source (SLS) at the Paul Scherrer Institute (PSI), Switzerland. In a typical experiment a small quantity of material was pressed onto an indium foil and fixed to a copper plate.[42] XAS measurements were performed in fluorescence mode. The X-ray fluorescence signal was detected using a 1-element Si-drift diode detector SDD (Ketek, Germany). Total electron yield was also collected in the case of Al K-edge measurements. In samples with a high content of absorbing atoms, *i.e.* non-diluted and not thin enough samples, the fluorescence detected XAS signal was corrected due to self-absorption. The current of the incoming beam (I_0) was measured using the total electron yield signal from a 0.5 μm thin polyester foil that was coated with a 50 nm thick layer of nickel. The beam passed through this foil approximately 1 m upstream of the sample in a vacuum chamber held at $\sim 10^{-6}$ mbar. Self-absorption correction in the Al K-edge spectra was applied. The Fe K-edge XAS spectra were collected at the BM31 beamline at the ESRF, Grenoble, France. The samples were ground, mixed with cellulose to optimize for X-ray absorption and pelletized. The data were collected in transmission mode using a Si(111) double crystal monochromator. Post-processing, self-absorption correction and analysis of the XAS data were performed using the Demeter 0.9.20 software package.[43]

High-resolution field emission scanning electron microscopy (Zeiss ULTRA 55 plus) was employed to visualize the surface morphology of the oxygen carriers before and after cyclic redox tests. Furthermore, elemental mapping of the synthesized materials was achieved *via* a Leo Gemini 1530 SEM equipped with an energy dispersive X-ray spectrometer (EDX). A FEI Talos F200X operated at 200 kV was used in both transmission electron microscopy (TEM) and scanning TEM (STEM) modes, with a probe size of approximately 0.8 nm. The instrument is equipped with SuperX EDX comprising four SDD detectors. The STEM/EDX analyses were complemented with atomic number sensitive, high angle annular dark field (HAADF) STEM.

The surface area as well as the pore size distribution of the calcined oxygen carriers were determined using a Quantochrome NOVA 4000e N_2 adsorption analyser. The samples were degassed at 300 °C for two hours prior to the acquisition of the N_2 isotherms. The Brunauer–Emmett–Teller (BET)[44] and Barrett–Joyner–Halenda (BJH)[45] models were used to calculate, respectively, the surface area and the pore size distribution of the materials.

Redox performance

Cyclic redox experiments were performed in a packed bed reactor, as described in detail in a previous study.[23] The operating temperature was 800 °C to ensure a sufficiently high reduction rate allowing for a full reduction of Fe_2O_3 to Fe in the set time. A typical redox cycle consists of the following steps: (i) reduction in CO (10 vol% CO in N_2) for 15 minutes (1.5 L min^{-1}), (ii) purging with N_2 (1.5 L min^{-1}) for 1 minute, (iii)

oxidation of the reduced oxygen carrier with steam (23 vol% H_2O in N_2) for 7 minutes (1.94 L min^{-1}), (iv) purging with N_2 (1.5 L min^{-1}) for 1 minute, and (v) oxidation with 5 vol% O_2 in N_2 (2 L min^{-1}) for 5 minutes.

Results and discussion

First, we discuss the cyclic redox behaviour of the synthesized oxygen carriers to determine the effect of the addition of sodium on the redox performance of the materials. Subsequently, we probe in detail the structure of the oxygen carriers in the calcined stated and after exposure to 15 redox cycles to establish structure–performance correlations.

Cyclic redox performance

The cyclic redox performance of the oxygen carriers was assessed over 15 redox cycles in a packed bed reactor at 800 °C. In each cycle, the oxygen carriers were reduced in CO (10 vol% CO in N_2) and oxidized first in H_2O (23 vol% H_2O in N_2) and in a second step in O_2 (5 vol% O_2 in N_2). The concentration profiles of the off gases for the different oxygen carriers during redox cycling are given in Fig. S2.† For each cycle, the H_2 yield during steam oxidation was calculated by integrating the molar flow-rate of H_2 produced (obtained from off-gas concentration profiles) with respect to time by using eqn (7):[21]

$$N_{H_2} = \dot{N}_{N_2} \times \int \frac{y_{H_2}}{1 - y_{H_2}} dt \quad (7)$$

where N_{H_2} is the number of moles of H_2 produced, $\dot{N}_{N_2}$ is the molar flow rate of N_2, and y_{H_2} is mole fraction of H_2 in the gas leaving the packed bed.

The H_2 yield expressed as mmol H_2 per g of oxygen carrier as a function of cycle number is given in Fig. 1. The H_2 yield of FeAl decreased rapidly over 15 cycles from 12.7 mmol H_2 per g oxygen carrier in the first cycle, to 11.1 mmol H_2 per g oxygen carrier in the fifth cycle and to 6 mmol H_2 per g oxygen carrier in the fifteenth cycle. The addition of sodium enhanced the redox stability of FeAlNa1 and increased the H_2 yield compared to FeAl; however, from the eighth redox cycle onwards also for this material the H_2 yield started to decrease. A more pronounce stabilization effect was observed in FeAlNa5. The H_2 yield of FeAlNa5 was stable over 15 redox cycles and was close to the theoretically expected value of 13.3 mmol g^{-1} oxygen carrier. These results show that the introduction of sodium has a large impact on the cyclic behaviour of Al_2O_3 stabilized, Fe_2O_3-based oxygen carriers.

The effect of sodium on the reduction kinetics of iron oxide can be evaluated using the gas concentration profiles obtained in the first cycle. The concentration profiles of the off gases given in Fig. S3a,† show that FeAlNa1 and FeAlNa5 have very comparable reduction rates. The fractional conversion of the oxygen carriers tested are only marginally different in the first reduction step, which indicates that the presence of sodium does not affect appreciably the reduction kinetics of Fe_2O_3. The reduction characteristics of the oxygen carriers were assessed further by CO and H_2-TPR experiments (Fig. S4†). In the case of steam oxidation, in the first cycle the conversion of FeAl was faster than the conversion of FeAlNa1 and FeAlNA5 indicating that the addition of sodium does not have a positive impact on oxidation kinetics (Fig. S5†). Over cycling, the water splitting kinetics decreased for the deactivating oxygen carriers (Fig. S6†). However, the overall oxidation duration of FeAlNa5 is fairly unaffected by the cycle number.

To obtain insight into the origin of the improved redox stability of FeAlNa1 and FeAlNa5 compared to FeAl, the morphological and structural characteristics of the calcined and cycled materials (15 cycles) were probed by XRD, XAS and STEM/EDX.

Structure of the calcined and cycled oxygen carriers by XRD and XAS

Calcined oxygen carriers. XRD analysis confirms that the main crystalline component in all of the calcined materials is hematite α-Fe_2O_3 (Fig. 2a and Table S2†). Additionally, α-Al_2O_3 (corundum) is observed in FeAl and FeAlNa1. In the case of FeAlNa5, there are also reflections due to α-Al_2O_3 observable; however, with a very weak intensity. In addition, FeAlNa5 contains a third phase, *i.e.* Na-β-Al_2O_3 ($P6_3/mmc$ space group, Fig. 2b).[46] Rietveld refinement allowed us to quantify the fraction of the crystalline phases in the oxygen carriers and to determine the cell parameters of these phases. The unit cell parameters of α-Fe_2O_3 and α-Al_2O_3 are reported in Table S2† and did not change (within the experimental error) upon the addition of sodium (Fig. 2 and Table S2†). The fact that the cell parameters are invariant with the addition of Na suggests that sodium is not incorporated into the crystal structures of α-Fe_2O_3 or α-Al_2O_3. The determined cell parameters of Na-β-Al_2O_3 ($a = b = 5.6385$ Å and $c = 22.816$ Å) is in a good agreement with previous studies.[46–48] The weight fractions of α-Al_2O_3 in the calcined materials were determined as 27, 23 and 3 wt% for FeAl and FeAlNa1 and FeAlNa5 respectively, *i.e.* the fraction of α-Al_2O_3 decreased with increasing Na content. For FeAl and FeAlNa1, α-Fe_2O_3 balanced the phase composition of the oxygen carriers, amounting to, respectively, 73 and 77 wt% α-Fe_2O_3. For FeAlNa5, the refined phase composition was 82 wt% α-Fe_2O_3, 15 wt% Na-β-Al_2O_3 and 3 wt% α-Al_2O_3. The presence of Na-β-Al_2O_3 in FeAlNa1 was not evidenced by XRD, yet this might be due to limitations of XRD in determining phases of low concentrations and/or poor crystallinity. To obtain further insight into the effect of the addition on sodium on the phase composition and structure of the oxygen carriers, we turned to an element specific technique X-ray technique, *i.e.* XAS at the Fe, Na and Al K-edges.

First, we analysed the local environment around iron. Fe K-edge XANES (X-ray absorption near edge structure) spectra of the calcined oxygen carriers are provided in Fig. 2d. The spectra of all of the oxygen carriers contain the same features as the α-Fe_2O_3 reference. The EXAFS (extended X-ray absorption fine structure) functions and the corresponding Fourier transforms (FT) are given in Fig. S7† and further confirm that the local environment around Fe corresponds to the local Fe environment in α-Fe_2O_3 in all three calcined materials. Hence, the XAS

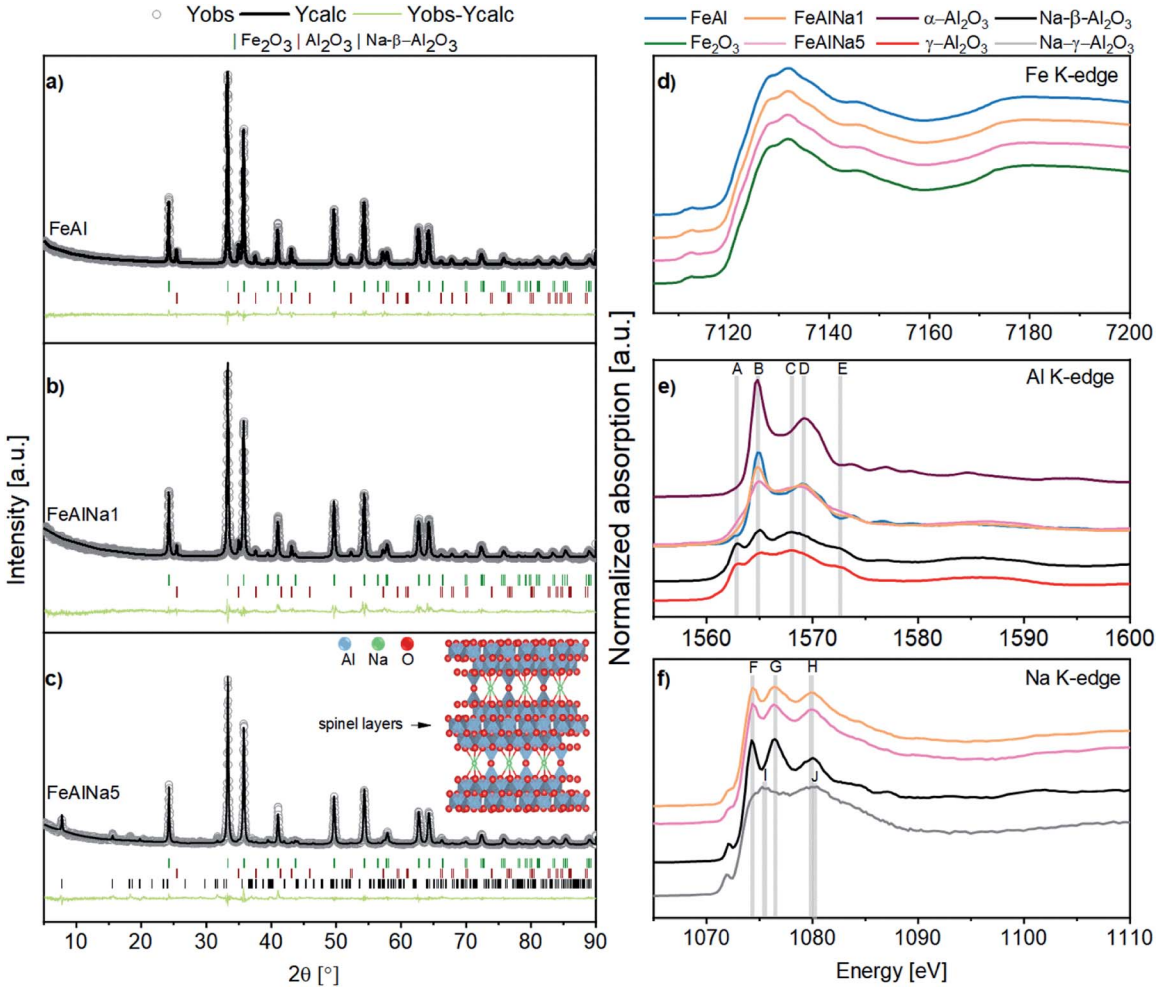

Fig. 2 (a)–(c) XRD patterns of the calcined oxygen carriers and the corresponding Rietveld refinements. The inset in (c) sketches the crystal structure of Na-β-Al_2O_3 containing layers of γ-alumina that are connected by bridging oxygen and sodium ions. XANES spectra at the (d) Fe K-edge, (e) Al K-edge, (f) Na K-edge of the calcined oxygen carriers and reference materials.

data confirm that the local environment of Fe is not affected by the presence of sodium. Importantly, it also shows that there is no formation of a solid solution or mixed oxide between Fe_2O_3 and Al_2O_3 upon calcination at 900 °C.

Fig. 2e displays the Al K-edge XANES spectra of the oxygen carriers and reference materials. To interpret these XANES data we will first discuss the XANES data of the reference materials α-Al_2O_3, γ-Al_2O_3 and Na-β-Al_2O_3. The crystal structure of α-Al_2O_3 is described by a hexagonal unit cell with Al in an octahedral coordination. The corresponding XANES spectrum (Fig. 2e) exhibits a doublet peak in the white-line region, with a sharp intense peak at 1565 eV (labelled as B), and a broader feature at 1568 eV (labelled as D), typical for Al in an octahedral coordination and in agreement with previously data.[49,50] The reference γ-Al_2O_3 has a defect spinel type structure, in which Al atoms occupy both octahedral and tetrahedral sites.[51] In the XANES spectrum of γ-Al_2O_3, features A, B, C and E are observed at 1563, 1565, 1568 and 1573 eV, respectively. In γ-Al_2O_3 feature B is considerably less intense than in α-Al_2O_3 and feature C has been attributed to tetrahedrally coordinated Al.[52,53] Na-β-Al_2O_3 is a layered structure containing γ-Al_2O_3 layers that are linked by sodium and oxygen atoms (inset in Fig. 2c).[54,55] The fact that the Al K-edge XANES spectrum of Na-β-Al_2O_3 exhibits similar features as γ-Al_2O_3 confirms the presence of γ-Al_2O_3 layers in Na-β-Al_2O_3.[54]

Next, we investigate the Al environment in the three oxygen carries. The Al K-edge XANES spectrum of FeAl shows features B and D, indicating that Al^{3+} is in an octahedral coordination similar to α-Al_2O_3,[49] in line with XRD. With increasing sodium content, the intensity of feature B decreases, which implies that the fraction of α-Al_2O_3 in the material decreases with increasing sodium content. In agreement with our previous XRD analysis is the fact that the Al K-edge XANES spectrum of FeAlNa1 is dominated by features due to α-Al_2O_3. On the other hand, in FeAlNa5 features A, C and E are prominent which is indicative of the presence of spinel-type γ-Al_2O_3 or Na-β-Al_2O_3 (according to XRD). Features A, C and E are also present in FeAlNa1, but with a considerably lower intensity. Hence, our XANES results indicate that FeAlNa1 and FeAlNa5 contain a mixture of α-Al_2O_3 and a spinel-type Al_2O_3 phase. While α-Al_2O_3 is the main Al-based phase in FeAlNa1, Na-β-Al_2O_3 (or γ-Al_2O_3) is the main Al-containing phase in FeAlNa5. Na-β-Al_2O_3 and γ-Al_2O_3 share

the same Al K-edge features, yet combining the information of XRD and Na-Kedge XAS (*vide infra*), we assign the observed features to Na-β-Al_2O_3 rather than to γ-Al_2O_3. Lastly, we assess the Na environment in the oxygen carriers and reference materials. The Na K-edge XANES spectrum of Na-β-Al_2O_3 exhibits three main peaks labelled as F, G and H, located at 1074, 1076 and 1080 eV, respectively (Fig. 2f). To the best of our knowledge, this is the first experimentally collected Na K-edge spectrum of Na-β-Al_2O_3. The spectrum of Na-γ-Al_2O_3 (*i.e.* the reference material prepared by wet impregnation of a solution of $NaNO_3$ onto γ-Al_2O_3) shows features different to Na-β-Al_2O_3 and are labelled I (1075 eV) and J (1080 eV) (Fig. S8†). These Na K-edge XANES features of Na-γ-Al_2O_3 are assigned to Na ions dispersed on the surface of γ-Al_2O_3 (in a solvated state).[55] Thus, using Na K-edge XANES we can distinguish between two different Na environments: (i) a Na-β-Al_2O_3 like environment, *i.e.* Na that is located between layers of γ-Al_2O_3 layers (ordered) and (ii) a Na-γ-Al_2O_3 like environment in which Na is located on the surface of γ-Al_2O_3 (surface Na^+). The Na K-edge XANES spectra of FeAlNa1 and FeAlNa5 exhibit features F, G and H at, respectively 1074.4 eV (A), 1076.4 eV (B) and 1080.2 eV (C), suggesting a similar Na local environment in these two calcined oxygen carriers as in Na-β-Al_2O_3 (Fig. 2f). The presence of Na-β-Al_2O_3 in FeAlNa5 aligns with XRD results. The absence of diffraction peaks due to Na-β-Al_2O_3 in FeAlNa1 is possibly linked to its small quantity in FeAlNa1. However, we noticed that the features F, G and H in the Na K-edge XANES spectra of FeAlNa1 and FeAlNa5 are less intense compared to the reference Na-β-Al_2O_3. This is possibly due to the presence of two different Na environments in the calcined oxygen carriers. This observation led us to propose that the Na K-edge XANES spectra of the oxygen carriers can be fitted by a linear combination of Na in an environment of Na-β-Al_2O_3 and surface Na^+ in the form of Na-γ-Al_2O_3. Indeed, linear combination fitting yielded Na to be *ca.* 60% in a Na-β-Al_2O_3 environment and 40% in a Na-γ-Al_2O_3 type environment in both FeAlNa1 and FeAlNa5 (Fig. S9†).

Cycled oxygen carriers. To probe in depth the effect of sodium-containing phases on the redox stability of the Fe_2O_3–Al_2O_3 system the structures of the oxygen carriers that have undergone 15 redox cycles were also characterized by XRD and XAS. The cycled oxygen carriers were analysed in their reduced state as it has been argued that the presence of sodium hinders the formation of inactive hercynite during reduction.[10,22,26]

The cycled materials (labelled with _cyc) exhibit dominant Bragg reflections due to fcc-Fe (Fig. 3a). However, the presence of magnetite (Fe_3O_4), wuestite-FeO (only in FeAl) and hercynite (spinel $FeAl_2O_4$) in $FeAl_{cyc}$ and $FeAlNa1_{cyc}$ points to an incomplete reduction. Importantly, the XRD pattern of $FeAlNa5_{cyc}$ does not show peaks due to $FeAl_2O_4$, but peaks due to Na-β-Al_2O_3 (Fig. 3a), indicating that Na-β-Al_2O_3 is stable under redox conditions. The XANES spectra and FT-EXAFS functions of the three cycled oxygen carriers are shown in Fig. 3 and S10,† respectively.

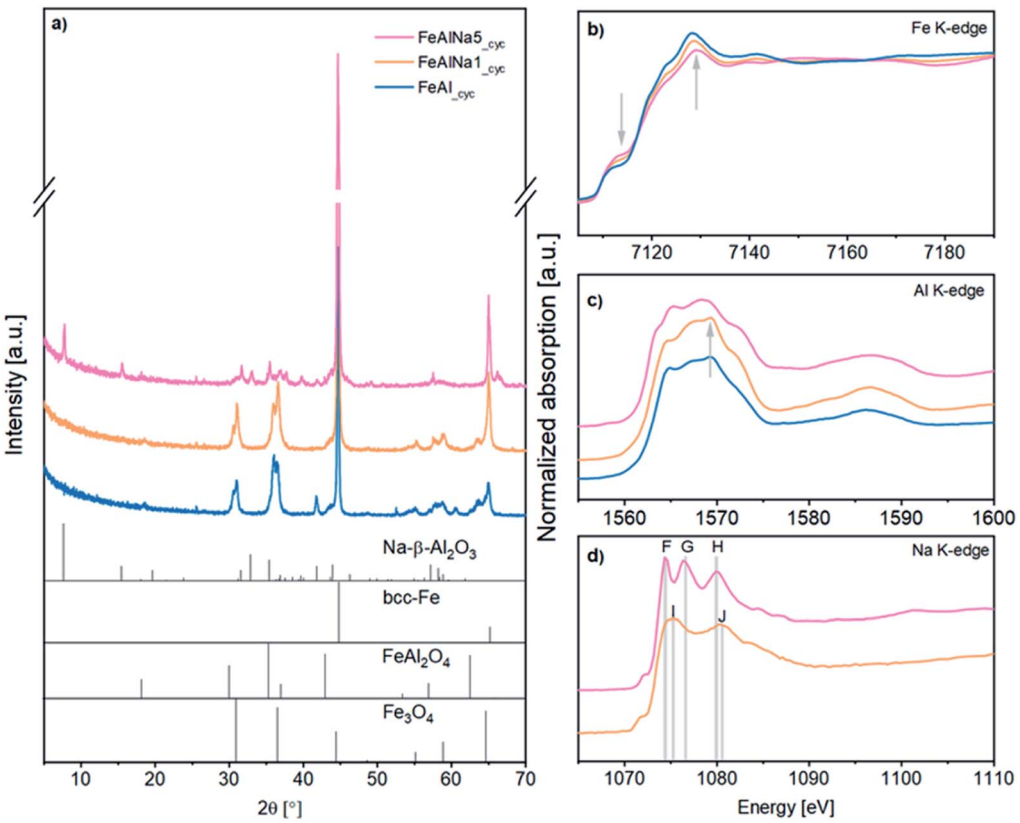

Fig. 3 (a) XRD patterns of the cycled oxygen carriers (15 redox cycles, reduction step) together with simulated diffraction patterns of the reference materials. XANES spectra at the (b) Fe K-edge (the arrows show the direction of change), (c) Al K-edge (the arrows point to distinct features in $FeAlNa_{cyc}$ and $FeAlNa_{cyc}$); and (d) Na K-edge of the cycled materials.

From the increase in the intensity of the white line it is clear that the degree of reduction followed the order $FeAl_{\_cyc}$ < $FeAlNa1_{\_cyc}$ < $FeAlNa1_{\_cyc}$. The Fe K-edge XANES spectra (Fig. 3b) of the oxygen carriers were fitted by a linear combination of an Fe foil, FeO and $FeAl_2O_4$ and yielded 48, 79 and 94 wt% metallic Fe^0 in, respectively, $FeAl_{\_cyc}$, $FeAlNa1_{\_cyc}$ and $FeAlNa5_{\_cyc}$. These results confirm that in FeAlNa5 the formation of $FeAl_2O_4$ during reduction is hindered and iron oxide can reduced almost completely over 15 redox cycles. To some extent, there is also a stabilization effect in FeAlNa1, yet the formation of $FeAl_2O_4$ could not avoided fully. This is line with the drop in the hydrogen yield of FeAlNa1 with cycle number.

Turning to the analysis of the Al K-edge XANES data of the cycled oxygen carriers, we did not observe any signatures due to α-Al_2O_3 in any of the cycled oxygen carriers, instead features characteristic of spinel type phases are present. The Al K-edge XANES spectrum of $FeAlNa5_{\_cyc}$ (Fig. 3c) shows the same characteristic features as the Na-β-Al_2O_3 reference (Fig. 2e). This indicates that during redox cycling the small fraction of α-Al_2O_3 that was initially present in calcined FeAlNa5 transforms fully to Na-β-Al_2O_3. Comparing the spectrum of $FeAlNa5_{\_cyc}$ with the spectra of $FeAl_{\_cyc}$ and $FeAlNa1_{\_cyc}$ revealed a more intense feature at *ca.* 1569.6 eV for $FeAl_{\_cyc}$ and $FeAlNa1_{\_cyc}$ (marked with an arrow in Fig. 3c). This feature can be attributed to the substitution of Al sites by Fe in a spinel structure in analogy to the spinel $MgAl_2O_4$ [52] which is isostructural to $FeAl_2O_4$. Hence, consolidating with our XRD and Fe K-edge XAS results, the feature at 1569.6 eV in the Al K-edge XANES spectra of $FeAl_{\_cyc}$ and $FeAlNa1_{\_cyc}$ is attributed to the formation of $FeAl_2O_4$.

The Na K-edge XANES spectra of the cycled materials are shown in Fig. 3d. We observe that in $FeAlNa5_{\_cyc}$ the local environment of Na in the form of Na-β-Al_2O_3 is preserved during redox cycling. This is evidenced by the presence of the three features F, G and H in $FeAlNa5_{\_cyc}$. Linear combination fitting of the spectrum of $FeAlNa5_{\_cyc}$ yields 71% of Na in a Na-β-Al_2O_3 framework and 29% of Na in the form of surface Na (Na-γ-Al_2O_3 type). Hence, the fraction of Na in a Na-β-Al_2O_3-type environment in FeAlNa5 increases with redox cycling, in line with Al K-edge XANES analysis. On the other hand, the Na K-edge XANES spectrum of $FeAlNa1_{\_cyc}$ exhibits, compared to FeAlNa5, a different change in the Na environmental with redox cycling. The three sharp features (labelled F, G and H) in calcined FeAlNa1 are not detected in $FeAlNa1_{\_cyc}$ (Fig. S11†). Instead a broader doublet (features I and J) at 1075 and 1080.5 eV appears after redox cycling, indicative that $FeAlNa1_{\_cyc}$ closely resembles the spectrum of the Na-γ-Al_2O_3 reference. This change in the local environment of Na upon redox cycling, indicates that in FeAlNa1 Na is initially present in a Na-β-Al_2O_3 like environment (in the layered structure), but migrates and disperses on the material's surface during redox cycling.

Morphology and elemental mapping of the calcined and cycled carriers

The morphology of the freshly calcined oxygen carriers, as probed by electron microscopy is affected only marginally by the addition of sodium (Fig. S12†). The calcined oxygen carriers FeAl, FeAlNa1 and FeAlNa5 were composed of particles with an average grain size of $\sim$100 $\pm$ 20 nm (based on the analysis of 50 particles). The particle size of Fe_2O_3, calculated using STEM-EDX maps of the calcined oxygen carries (Fig. S13†), was in the range of 80–120 nm for the oxygen carries tested (119 $\pm$ 33 nm, 135 $\pm$ 36 nm and 87 $\pm$ 40 nm for FeAl, FeAlNa1 and FeAlN5, respectively). The weight composition of the materials a determined by SEM/EDX (Table S1†) are in good agreement with the nominal compositions of the oxygen carriers. The elemental mapping of the oxygen carriers revealed that the sol–gel synthesis led to a high dispersion of Fe, Na and Al, indicating that the different phases were highly dispersed in the materials (Fig. S14†). The calcined oxygen carriers FeAl, FeAlNa1 and FeAlNa5 have similar BET surface areas and BJH pore volumes (Table S1†).

HAADF-STEM images and the corresponding EDX maps of Fe, Al and Na are given in Fig. 4. In the calcined materials FeAl, FeAlNa1, and FeAlNa5, discrete Fe_2O_3- and Al_2O_3-rich particles are formed, and Na is distributed evenly in FeAlNa1. In FeAlNa5, the EDX signals of Al and Na overlap, which is in line with the outcome of the XRD and XAS analysis (Fig. 2) pointing to the formation of a Na-β-Al_2O_3 phase. Similarly, the EDX maps of $FeAl_{\_cyc}$ and $FeAlNa1_{\_cyc}$ show overlapping signals of Fe and Al, which are in agreement with the formation of the spinel $FeAl_2O_4$ as determined by XRD and XAS. No such overlap is observed in $FeAlNa5_{\_cyc}$, which features discrete Al- and Fe-rich particles. Furthermore, the overlapping signals of Na and Al in $FeAlNa5_{\_cyc}$ provide further evidence for the formation of Na-β-Al_2O_3 as determined by the XRD and XAS analyses.

Structure–performance relationships

Combing the results of the cyclic redox tests, with our XRD, XAS and HAADF-STEM-EDX analyses we can propose the following structure–performance correlations. The reaction of α-Al_2O_3 with Fe/FeO_x during redox cycling leads to the formation of (inactive) $FeAl_2O_4$ that in turn correlates with a rapid decay in the H_2 yield in FeAl. The high redox stability of FeAlNa5 correlates with the formation of Na-β-Al_2O_3 and the absence of α-Al_2O_3 in this oxygen carrier. The formation of Na-β-Al_2O_3 in FeAlNa5 hinders effectively the formation of $FeAl_2O_4$ during repeated redox cycles, leading in turn to a material with a stable hydrogen yield. The Na-β-Al_2O_3 phase is stable at reductive and oxidative environments and is highly dispersed within the Fe/FeO_x matrix. The oxygen carrier with a lower Na content, *i.e.* FeAlNa1, shows a dominating presence of α-Al_2O_3 and a small fraction of Na-β-Al_2O_3 initially freshly calcined state. Such a phase composition can only partially stabilize the oxygen carrier. Indeed, in FeAlNa1, Na is initially present in two environments *i.e.* as Na-β-Al_2O_3 and dispersed as surface Na. During the redox cycling of FeAlNa1, all of the α-Al_2O_3 reacts with FeO_x forming $FeAl_2O_4$, while sodium is found in a non-crystalline form (dispersed at the surface of the particle). A schematic representation of the phase evolution during redox cycling is given in Fig. S15.† Therefore, our study points to the critical role of the layered Na-β-Al_2O_3 phase in stabilizing the hydrogen yield of Al_2O_3-stabilized, Fe_2O_3 based oxygen carriers.

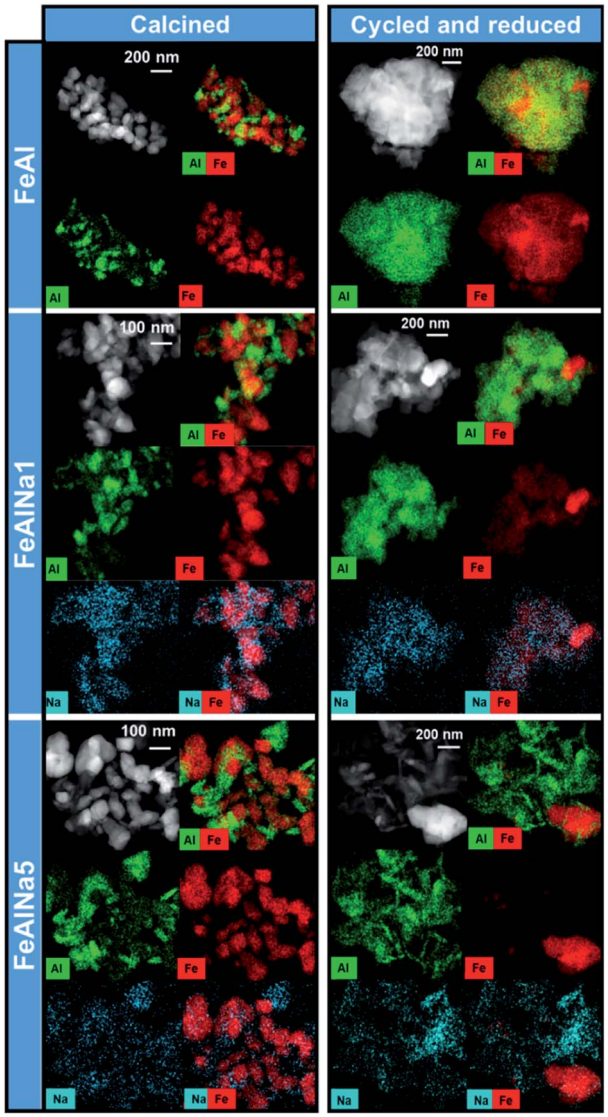

Fig. 4 HAADF images and elemental maps (STEM-EDX) of the calcined oxygen carriers and after cycling experiments (15 cycles, reduction step).

Conclusions

In this work, we probe the effect of the addition of sodium to Fe_2O_3–Al_2O_3-based oxygen carriers, on their redox stability, phase composition and phase dynamics over redox cycles. Application of XRD, XAS at the Al, Na and Fe K-edges and STEM/EDX to the freshly calcined and cycled materials allowed us to draw the following conclusions:

(i) α-Al_2O_3 reacts with Fe/FeO_x during redox cycling leading to the formation of $FeAl_2O_4$; the formation of which correlates directly with the rapid decrease in the H_2 yield of an oxygen carrier.

(ii) Depending on the loading of sodium in the oxygen carrier, sodium can be found in a crystalline Na-β-Al_2O_3 phase or at the surfaces of the particles.

(iii) Na in the environmental of the layered structure Na-β-Al_2O_3 effectively stabilizes the redox performance of an oxygen carrier, while surface sodium cannot prevent fully material deactivation.

This work, demonstrates how probing of the local and average structure, such as multi edge XAS analysis in combination with XRD and electron microscopy allows for the formulation of structure–performance correlations. In addition, this work showcases the application of XAS in the tender X-ray region (Na and Al K-edges) that have not been investigated extensively particularly in the field of chemical looping and can, therefore, be of interest to the broader functional materials community. Our study brings fundamental understanding of the role of Na-β-Al_2O_3 for the stabilization of Fe_2O_3-based oxygen carriers. Nonetheless, further studies that explore different reducing gases (such as CH_4), operation temperatures and long-term stability (>100 cycles) are required.

Conflicts of interest

There are no conflicts to declare.

Acknowledgements

The authors would like to acknowledge the Swiss National Science Foundation (406640_136707) and the Swiss Office of Energy (BFE, SI/500652) for financial support. This project has received partial funding from the European Union's Horizon 2020 research and innovation program (grant agreement No. 800419). This publication was created as part of NCCR Catalysis, a National Centre of Competence in Research funded by the Swiss National Science Foundation. We also thank Scientific Centre for Optical and Electron Microscopy (ScopeM) for providing training and access to scanning electron microscopes. The authors are grateful to the Swiss Light Source (SLS) at the Paul Scherrer Institute (Villigen, Switzerland), for providing beamtime at the PHOENIX beamline, and to the European Synchrotron Facility (ESRF) and the Swiss-Norwegian beamline (SNBL at ESRF) for providing beamtime for XAS measurements. We thank Dr Felix Donat for the insightful discussions on thermodynamic analysis.

Notes and references

1 BP, *Energy Outlook 2017 Edition*, 2017.
2 IEA, *Technology Roadmap: Hydrogen and Fuel Cells*, 2015.
3 J. A. Turner, *Science*, 2004, **305**, 972–974.
4 M. Zerta, P. R. Schmidt, C. Stiller and H. Landinger, *Int. J. Hydrogen Energy*, 2008, **33**, 3021–3025.
5 T. V. Choudhary and D. Goodman, *Catal. Today*, 2002, **77**, 65–78.
6 G. Postole and A. Auroux, *Int. J. Hydrogen Energy*, 2011, **36**, 6817–6825.
7 C. Bohn, J. Cleeton, C. Müller, S. Chuang, S. Scott and J. Dennis, *Energy Fuels*, 2010, **24**, 4025–4033.
8 A. Thursfield, A. Murugan, R. Franca and I. S. Metcalfe, *Energy Environ. Sci.*, 2012, **5**, 7421–7459.

9 Q. Zafar, T. Mattisson and B. Gevert, *Ind. Eng. Chem. Res.*, 2005, **44**, 3485–3496.
10 P. R. Kidambi, J. P. E. Cleeton, S. A. Scott, J. S. Dennis and C. D. Bohn, *Energy Fuels*, 2012, **26**, 603–617.
11 J. R. Scheffe, M. D. Allendorf, E. N. Coker, B. W. Jacobs, A. H. McDaniel and A. W. Weimer, *Chem. Mater.*, 2011, **23**, 2030–2038.
12 R. D. Solunke and G. Veser, *Ind. Eng. Chem. Res.*, 2010, **49**, 11037–11044.
13 N. S. Yüzbasi, P. M. Abdala, Q. Imtiaz, S. M. Kim, A. M. Kierzkowska, A. Armutlulu, W. van Beek and C. R. Müller, *Phys. Chem. Chem. Phys.*, 2018, **20**, 12736–12745.
14 L.-S. Fan and F. Li, *Ind. Eng. Chem. Res.*, 2010, **49**, 10200–10211.
15 G. Voitic and V. Hacker, *RSC Adv.*, 2016, **6**, 98267–98296.
16 M. Rydén and M. Arjmand, *Int. J. Hydrogen Energy*, 2012, **37**, 4843–4854.
17 C. D. Bohn, C. R. Müller, J. P. Cleeton, A. N. Hayhurst, J. F. Davidson, S. A. Scott and J. S. Dennis, *Ind. Eng. Chem. Res.*, 2008, **47**, 7623–7630.
18 J. P. E. Cleeton, C. D. Bohn, C. R. Müller, J. S. Dennis and S. A. Scott, *Int. J. Hydrogen Energy*, 2009, **34**, 1–12.
19 D. Hosseini, F. Donat, S. M. Kim, L. Bernard, A. M. Kierzkowska and C. R. Müller, *ACS Appl. Energy Mater.*, 2018, **1**, 1294–1303.
20 W.-C. Huang, Y.-L. Kuo, P.-C. Su, Y.-H. Tseng, H.-Y. Lee and Y. Ku, *Chem. Eng. J.*, 2018, **334**, 2079–2087.
21 Q. Imtiaz, N. S. Yüzbasi, P. M. Abdala, A. M. Kierzkowska, W. van Beek, M. Broda and C. R. Müller, *J. Mater. Chem. A*, 2016, **4**, 113–123.
22 A. Kierzkowska, C. Bohn, S. Scott, J. Cleeton, J. Dennis and C. Muller, *Ind. Eng. Chem. Res.*, 2010, **49**, 5383–5391.
23 W. Liu, J. S. Dennis and S. A. Scott, *Ind. Eng. Chem. Res.*, 2012, **51**, 16597–16609.
24 C. Müller, C. Bohn, Q. Song, S. Scott and J. Dennis, *Chem. Eng. J.*, 2011, **166**, 1052–1060.
25 J. B. Yang, N. S. Cai and Z. S. Li, *Energy Fuels*, 2008, **22**, 2570–2579.
26 N. S. Yüzbasi, A. Kierzkowska and C. Müller, *Energy Procedia*, 2017, **114**, 436–445.
27 N. S. Yüzbasi, A. M. Kierzkowska, Q. Imtiaz, P. M. Abdala, A. Kurlov, J. L. M. Rupp and C. R. Müller, *J. Phys. Chem. C*, 2016, **120**, 18977–18985.
28 Z. Ma, S. Zhang and R. Xiao, *Energy Convers. Manage.*, 2019, **188**, 429–437.
29 M. Ishida, K. Takeshita, K. Suzuki and T. Ohba, *Energy Fuels*, 2005, **19**, 2514–2518.
30 C. Chung, L. Qin, V. Shah and L.-S. Fan, *Energy Environ. Sci.*, 2017, **10**, 2318–2323.
31 W. Liu, M. Ismail, M. T. Dunstan, W. Hu, Z. Zhang, P. S. Fennell, S. A. Scott and J. S. Dennis, *RSC Adv.*, 2015, **5**, 1759–1771.
32 M. Arjmand, A.-M. Azad, H. Leion, T. Mattisson and A. Lyngfelt, *Ind. Eng. Chem. Res.*, 2012, **51**, 13924–13934.
33 J. Adanez, A. Abad, F. Garcia-Labiano, P. Gayan and L. F. de Diego, *Prog. Energy Combust. Sci.*, 2012, **38**, 215–282.
34 Q. Imtiaz, P. M. Abdala, A. M. Kierzkowska, W. Van Beek, S. Schweiger, J. L. Rupp and C. R. Müller, *Phys. Chem. Chem. Phys.*, 2016, **18**, 12278–12288.
35 A. Turnock and H. Eugster, *J. Petrol.*, 1962, **3**, 533–565.
36 K. J. Warren, J. T. Tran and A. W. Weimer, *Energy Environ. Sci.*, 2022, **15**, 806–821.
37 C. L. Muhich, B. W. Evanko, K. C. Weston, P. Lichty, X. Liang, J. Martinek, C. B. Musgrave and A. W. Weimer, *Science*, 2013, **341**, 540–542.
38 C. L. Muhich, B. D. Ehrhart, V. A. Witte, S. L. Miller, E. N. Coker, C. B. Musgrave and A. W. Weimer, *Energy Environ. Sci.*, 2015, **8**, 3687–3699.
39 Q. Song, W. Liu, C. D. Bohn, R. N. Harper, E. Sivaniah, S. A. Scott and J. S. Dennis, *Energy Environ. Sci.*, 2013, **6**, 288–298.
40 L. Liu and M. R. Zachariah, *Energy Fuels*, 2013, **27**, 4977–4983.
41 J. Rodriguez-Carvajal, *Phys. B*, 1993, **192**, 55.
42 M. Galib, M. Baer, L. Skinner, C. Mundy, T. Huthwelker, G. Schenter, C. Benmore, N. Govind and J. L. Fulton, *J. Chem. Phys.*, 2017, **146**, 084504.
43 B. Ravel and M. Newville, *J. Synchrotron Radiat.*, 2005, **12**, 537–541.
44 S. Brunauer, P. H. Emmett and E. Teller, *J. Am. Chem. Soc.*, 1938, **60**, 309–319.
45 E. P. Barrett, L. G. Joyner and P. P. Halenda, *J. Am. Chem. Soc.*, 1951, **73**, 373–380.
46 N. Zhu, F. Guo, S. Yan, L. Chen and A. Li, *Acta Chim. Sin.*, 1992, **50**, 527–532.
47 W. A. England, A. J. Jacobson and B. C. Tofield, *Solid State Ionics*, 1982, **6**, 21–27.
48 C. Peters, M. Bettman, J. t. Moore and M. Glick, *Acta Crystallogr., Sect. B: Struct. Crystallogr. Cryst. Chem.*, 1971, **27**, 1826–1834.
49 A. Omegna, R. Prins and J. A. van Bokhoven, *J. Phys. Chem. B*, 2005, **109**, 9280–9283.
50 D. R. Neuville, L. Cormier, A.-M. Flank, V. Briois and D. Massiot, *Chem. Geol.*, 2004, **213**, 153–163.
51 R. Prins, *J. Catal.*, 2020, **392**, 336–346.
52 D. R. Neuville, D. De Ligny, L. Cormier, G. S. Henderson, J. Roux, A.-M. Flank and P. Lagarde, *Geochim. Cosmochim. Acta*, 2009, **73**, 3410–3422.
53 Y. Kato, K.-i. Shimizu, N. Matsushita, T. Yoshida, H. Yoshida, A. Satsuma and T. Hattori, *Phys. Chem. Chem. Phys.*, 2001, **3**, 1925–1929.
54 A. Marcelli, A. Mottana and G. Cibin, *J. Appl. Crystallogr.*, 2000, **33**, 234–242.
55 M. Digne, P. Raybaud, P. Sautet, D. Guillaume and H. Toulhoat, *Phys. Chem. Chem. Phys.*, 2007, **9**, 2577–2582.

